Verwey Transition under Oxygen Loading in RBaFe$_2$O$_{5+w}$ (R = Nd and Sm)

P. Karen,*,[1] P. M. Woodward,† P. N. Santhosh,† T. Vogt,‡ P. W. Stephens,§ and S. Pagola§

*Department of Chemistry, University of Oslo, P.O.Box 1033 Blindern, N-0315 Oslo, Norway; †Department of Chemistry, The Ohio State University, 100 West 18th Avenue, Columbus, Ohio 43210-1185; ‡Physics Department, Brookhaven National Laboratory, Upton, New York 11973-5000; and §Department of Physics and Astronomy, State University of New York at Stony Brook, Stony Brook, New York 11794-3800

Double-cell perovskites RBaFe$_2$O$_{5+w}$ (R = Nd and Sm) are synthesized in the $-0.03 < w < 0.47$ portion of the nonstoichiometry range. The ideal composition with $w = 0$ has di- and trivalent iron in equal proportions and exhibits a charge-ordering Verwey transition upon cooling, preceded by a weaker premonitory transition. Both transitions are detectable by differential scanning calorimetry. The changes in entropy, volume, orthorhombic distortion and electrical conductivity at the main transition are larger for the variant with the smaller Sm atom than for R = Nd. The discontinuity of the SmBaFe$_2$O$_{5+w}$ transition also persists into much higher levels of the oxygen nonstoichiometry w than for the R = Nd variant. Whereas 3D-charge-ordered SmBaFe$_2$O$_{5.00}$ is isostructural with TbBaFe$_2$O$_{5.00}$ adopting space group *Pmma*, NdBaFe$_2$O$_{5.00}$ undergoes a more profound structural change upon entering the charge-ordered state, the structure of which is refined in the *P2$_1$ma* symmetry from high-resolution X-ray synchrotron diffraction data. © 2002 Elsevier Science (USA)

Key Words: mixed valence; charge ordering.

1. INTRODUCTION

The Verwey transition (1,2) in magnetite, Fe$_3$O$_4$, is one of the earliest known examples of charge ordering in a transition metal oxide. Whereas at ambient temperature the octahedral spinel sublattice is occupied by a single mixed-valence state Fe$^{2.5+}$, below $T_V = 120$ K an ordered distribution (3) of di- and tri-valent iron appears, accompanied by a sudden rise in electrical resistivity. The charge ordering can be directly evidenced by Mössbauer spectroscopy (4) and near-edge anomalous X-ray scattering (5). The transition is of the first order, but this attribute applies only to a small nonstoichiometry range with respect

[1] To whom correspondence should be addressed. Fax: +47-22-85-54-41. E-mail: pavel.karen@kjemi.uio.no.

to both oxygen and aliovalent dopants (6,7). Attempts have been made (8–13) to present a theoretical model dealing with both the first- and higher-order Verwey transition. These mean-field approximations describe the transition as an entropy-driven ordering accompanied by a volume effect. The Coulombic stabilization is also believed to be the main ingredient of a similar transition in Fe$_2$OBO$_3$ which remains a paramagnetic insulator (magnetic $T_C = 155$ whereas $T_V = 317$ K), and shows only a modest change in electrical conductivity (14). A formal replacement of the tetrahedral Fe^{3+} in magnetite by yttrium (or similar rare-earth elements) leads to rhombohedral YFe$_2$O$_4$ which exhibits Verwey transition around 200 K, this time on the background of an antiferromagnetic (AFM) arrangement. It is interesting to note that *molecular* iron oxides where various organic ligands stabilize the same valence states in the same ratio as in magnetite (trinuclear iron complexes) undergo an analogous transition where two Fe–O bonds become unequal at low temperatures whereas the third bond does not participate (15,16). Finally we note that a number of nonoxide iron compounds exhibit Fe^{II}/Fe^{III} mixed valence. These range from Prussian Blue to Fe–S clusters of biologically important ferredoxins.

Recently, a mixed-valence state Fe$^{2.5+}$ was observed in SmBaFe$_2$O$_5$ by Mössbauer spectroscopy (17). It occupies identical square-pyramidally coordinated sites created by an oxygen vacancy residing in the Sm layer of the double-cell perovskite-type structure (18). Upon completing the transition on cooling, the Fe$^{2.5+}$ Mössbauer component disproportionates fully into the integer Fe^{3+} and Fe^{2+} valence states. The crystal and magnetic structures of the charge-ordered phase have been solved from powder neutron and synchrotron X-ray diffraction data on the TbBaFe$_2$O$_5$ variant (19). The results show that the charge-ordering transition is accomplished in two steps. A "premonitory" step, as high as 30 K above the main

transition, creates two mixed-valence states, $Fe^{2.5+\varepsilon}$ and $Fe^{2.5-\varepsilon}$. The main step, a classical Verwey-type transition, then accomplishes the ordering into practically integer charges. In the charge-ordered state all of the nearest-neighbor Fe–Fe interactions are AFM, whereas the mixed-valence state is characterized by a ferromagnetic (FM) Fe–Fe coupling across the R layer. This behavior suggests a correlation between the electron localization, the magnetic interactions and the properties of the R atom present.

In this study, two R variants, Nd and Sm, are investigated. Unlike $R = $ Tb, these variants allow for a wide oxygen nonstoichiometry to occur in the crystal structure. Here we report the effect of the oxygen nonstoichiometry on the Verwey-type transition as studied by calorimetry, X-ray powder diffraction and magnetometry.

2. EXPERIMENTAL

Syntheses. Samples of $R\text{BaFe}_2\text{O}_{5+w}$ with controlled oxygen content were obtained via equilibration and quenching from well-sintered master samples synthesized from nanoscale precursors. The starting materials were iron lumps (99.95%, Koch-Light) dissolved in advance in diluted HNO_3, sesquioxides of neodymium (99.9%, Acros) and samarium (99.99%, Merck), barium carbonate (0.1% Sr, Merck) and citric acid monohydrate (reagent grade, Merck). The nanoscale precursor was obtained in the following steps: (i) standardized rare-earth oxides were dry-mixed with 20 mol of citric acid monohydrate per mol R and dissolved upon melting assisted by a small amount of water, (ii) the iron nitrate solution was gradually added into the stirred citrate melt under cautious heating until cessation of nitrous gasses, (iii) the melt was cooled below 100°C, and its volume was increased by 50% by adding redistilled water followed by dissolution of the barium carbonate, (iv) upon evaporation of some water a clear, orange-brown, viscous melt was obtained and subsequently decomposed into an organic-based porous solid (a xerogel) at 180°C and (v) the solid was milled in a vibration mill, compacted into a porcelain crucible, covered with a lid and slowly incinerated over several days in air at 400°C. The nanoprecursors were then calcined for 20 h at 900°C in a wet ($p_{\text{H}_2\text{O}} = 0.022$ bar) atmosphere of argon and hydrogen premixed 80:1 by volume. The calcinates were single phase, with broad Bragg peaks. Conditions for the subsequent 20-h sintering into $>95\%$ dense samples (cold-pressed under 150 kg/cm^2) have been tested in separate experiments and are summarized in Table 1. It is important to note that the achieved degree of sintering must be attributed to the nanoscale precursor; powders calcined twice sinter to only $\sim 80\%$ density, whereas milled powder that has already been sintered reaches no more than 60% density under conditions listed

TABLE 1
Synthesis Conditions of $R\text{BaFe}_2\text{O}_{5+w}$ Master Samples (Pressures in Bars, Ar:H$_2$ by Volume)

R	t (°C)	$\log p_{\text{O}_2}$	$p_{\text{H}_2\text{O}}$	Ar:H$_2$
Nd	1040	−14.54(1)	0.024	16.7(2)
Sm	1020	−14.88(2)	0.022	16.7(5)

in Table 1. Synthesized samples were single phase by synchrotron powder X-ray diffraction.

Oxygen content control. The content of oxygen in the solid was defined by temperature and partial pressure of oxygen under the high-temperature equilibrium (20,21) in the atmosphere of Ar, H_2 and H_2O. After 5–7 days of equilibration, samples were quenched into a bulk metal container filled with high-purity Ar (<2 ppm O_2, dried over a P_2O_5 desiccant). The compact samples were stored under Ar and a thin surface layer was removed before further characterizations (Table 2).

Oxygen content analyses. The oxygen content was determined by cerimetric titration, described in detail in Ref. (18). Each titration was performed in duplicate or triplicate. For results see Table 2.

Conventional X-ray powder diffraction (XPD). The phase purity and unit-cell parameters were evaluated from XPD data obtained with a Guinier–Hägg camera with $CuK\alpha_1$ radiation and Si as an internal standard. The photographs were scanned by a Nicolet LS-18 film scanner with the SCANPI software (22).

Synchrotron X-ray powder diffraction (SXPD). Data were collected at the National Synchrotron Light Source located at Brookhaven National Laboratory, on powdered samples in Ar-filled glass capillaries of diameter typically 0.25 mm. Radiation with wavelengths around 0.7 Å was used, each time calibrated on a NIST corundum X-ray diffraction standard. Low-temperature data for the series of nonstoichiometric samples were collected at 70 K at the X3B1 beamline on a powder diffractometer equipped with cryostat, Ge(111) analyzer and a scintillation detector. Scans up to typically 40° in 2θ with the step size of 0.004°, counting time 4 s and 5° rotation per step were performed. Upon cooldowns, repetitive short scans across the 100, 010, 002 or 110, 102, 012 peaks were collected in order to get an overall picture of the effects of temperature and non-stoichiometry upon the unit-cell parameters and phase transitions. Data were also collected at the X7A beamline at both 15 K for refinement of the charge-ordered super-structure and as a function of temperature up to 400 K. These data were collected using a closed-cycle model CSW-202 displex cryofurnace (Advanced Research Systems, Inc.)

TABLE 2
Oxygen Content Control and Characterizations of the $R\text{BaFe}_2\text{O}_{5+w}$ Samples Used

R	$5+w$	a	b	c	Ar/H_2	$\log p_{H_2O}$	$\log p_{O_2}$	t
Nd	4.977(1)	3.9705(7)	3.9594(7)	7.6440(13)	9.19	−4.0	−27.5	670
Nd	4.984(1)	3.9716(5)	3.9608(5)	7.6458(9)	8.78	−4.1	−27.9	660
Nd	5.004(1)	3.9705(10)	3.9607(10)	7.6469(16)	8.78	−4.1	−28.2	650
Nd	5.010(1)	3.9736(7)	3.9598(7)	7.6487(16)	9.19	−4.0	−27.9	655
Nd	5.012(1)	3.9705(8)	3.9604(8)	7.6425(15)	9.19	−4.0	−28.1	650
Nd	5.027(1)	3.9692(4)	3.9609(4)	7.6491(8)	4.13	−1.70	−16.41(5)	1000
Nd	5.036(2)	3.9686(5)	3.9607(6)	7.6511(12)	1.71	−1.69	−18.30(8)	920
Nd	5.053(3)	3.9656(3)		7.6526(7)	5.35	−1.65	−15.49(2)	1040
Nd	5.056(1)	3.9663(4)		7.6523(14)	3.40	−1.65	−17.06(3)	960
Nd	5.079(2)	3.9637(4)		7.6607(8)	9.00	−1.66	−15.74(4)	1000
Nd	5.087(1)	3.9644(2)		7.6584(7)	9.16	−1.60	−14.98(3)	1040
Nd	5.138(3)	3.9613(3)		7.6783(10)	16.7	−1.67	−15.28(1)	1000
Nd	5.192(2)	3.9604(3)		7.6939(9)	27.5	−1.66	−14.84(3)	1000
Nd	5.239(1)	3.9595(2)		7.7071(5)	31.8	−1.64	−14.66(1)	1000
Nd	5.264(2)	3.9589(2)		7.7145(5)	41.3	−1.62	−14.41(3)	1000
Nd	5.296(1)	3.9572(4)		7.7214(11)	83.2	−1.64	−13.85(6)	1000
Nd	5.357(1)	3.9557(2)		7.7371(6)	124	−1.62	−13.46(1)	1000
Nd	5.402(1)	3.9529(2)		7.7467(7)	282	−1.64	−12.78(3)	1000
Nd	5.467(1)	3.9498(3)		7.7638(9)	1790	−1.68	−11.11(6)	1000
Sm	4.980(1)	3.9626(4)	3.9455(4)	7.6092(7)	8.78	−4.1	−27.6	670
Sm	4.999(3)	3.9626(5)	3.9450(5)	7.6120(11)	8.65	−4.4	−29.3	630
Sm	5.002(1)	3.9625(6)	3.9453(6)	7.6108(10)	8.65	−4.2	−28.6	640
Sm	5.007(2)	3.9617(6)	3.9442(5)	7.6110(11)	8.65	−4.3	−29.4	620
Sm	5.014(4)	3.9620(4)	3.9458(4)	7.6119(7)	8.78	−4.1	−27.9	660
Sm	5.016(1)	3.9627(6)	3.9464(6)	7.6122(8)	8.78	−4.1	−28.2	650
Sm	5.022(1)	3.9616(6)	3.9435(6)	7.6174(11)	8.78	−4.1	−28.5	640
Sm	5.030(3)	3.9589(6)	3.9479(5)	7.6214(10)	16.3	−1.68	−15.31(1)	1000
Sm	5.064(1)	3.9528(3)		7.6277(8)	24.9	−1.67	−14.93(3)	1000
Sm	5.095(2)	3.9515(6)		7.6361(16)	41.3	−1.68	−14.53(1)	1000
Sm	5.137(1)	3.9494(2)		7.6494(8)	74.2	−1.68	−14.03(2)	1000
Sm	5.142(2)	3.9504(2)		7.6545(14)	83.2	−1.64	−13.85(2)	1000
Sm	5.182(3)	3.9487(4)		7.6644(11)	101	−1.68	−13.76(1)	1000
Sm	5.202(4)	3.9474(2)		7.6713(6)	137	−1.69	−13.51(5)	1000
Sm	5.249(1)	3.9463(3)		7.6865(9)	238	−1.66	−12.96(1)	1000
Sm	5.320(1)	3.9426(3)		7.7049(7)	398	−1.62	−12.44(4)	1000
Sm	5.346(2)	3.9433(3)		7.7143(8)	341	−1.65	−12.64(6)	1000

Note. Cell parameters in Å, ratio Ar/H_2 by volume, pressures in bars, temperature t in °C. Standard errors referring to mixing are listed when variations over time were evaluated.

operable in the temperature range of 15–750 K. Short isothermal scans were collected over the angular range 9–22° (2θ), extended scans were collected between 9° and 70° (2θ), using a multiwire linear position-sensitive detector filled with Kr. Structural refinements were performed using the Rietveld method as implemented in the GSAS software suite (23). Absorption correction was applied based on the estimated density of the powder in the capillary; the μR values were close to 1. A linear interpolation between fixed points was used to model the background.

Magnetic susceptibility. Magnetic susceptibility data were collected with a Magnetic Properties Measurement System (MPMS; Quantum Design) SQUID apparatus. Measurements were performed upon heating (zero-field-cooled samples) between 5 and 300 K using a measurement field of 500 Oe. The approximately 50 mg samples were in

one solid piece of approximately spherical shape. Data for temperatures between 300 and 750 K were obtained by the Faraday method, in a field-independent region (10 kOe maximum) with a 15 mg sample sealed in evacuated silica-glass ampoules.

Differential scanning calorimetry (DSC). A Perkin-Elmer Pyris 1 differential scanning calorimeter operated with liquid nitrogen was used to register thermal flux curves upon heating at a rate of 10 K/min between 120 and 340 K. Coarsely powdered samples (50–140 mg) were sealed in aluminum pans, and the effect of their mass on the peak temperatures was calibrated. The temperature scale was calibrated with following standards of >99.7% purity: cyclopentane, cyclohexane, *n*-octane, *n*-decane, *n*-dodecane, *m*-nitrotoluene and *p*-nitrotoluene. The heat effect was calibrated on melting of the (Perkin–Elmer)

standard indium and a HPLC-grade cyclohexane. Enthalpies were obtained by integration, after subtraction of the background approximated by suitable polynomials according to the least-squares method.

Electrical conductivity. Measurements were carried out on rectangular pellets ($\sim 1 \times 2 \times 4 \, \text{mm}^3$) using linear four-probe method. A Keithley 195A Digital Multimeter and a Keithley 200 Current Source were used for this purpose. The electrical contacts were given using carbon paint to avoid any offset values observed in the case of silver paint contacts. The measurements were done from room temperature to lower temperatures (the experiments were

stopped when the resistivity values became too large to be measured using our setup) in a liquid-helium cryostat.

3. RESULTS

3.1. Verwey-type Transition

The most sensitive detection of the transition between the integer and mixed-valence charges in $R\text{BaFe}_2\text{O}_{5+w}$ is provided by DSC. Close to the zero oxygen nonstoichiometry ($w = 0$), also the weak first attempt to order charges is registered (Fig. 1) as it was for $R = $ Tb in Ref. (19). Despite the considerable distance between the two transi-
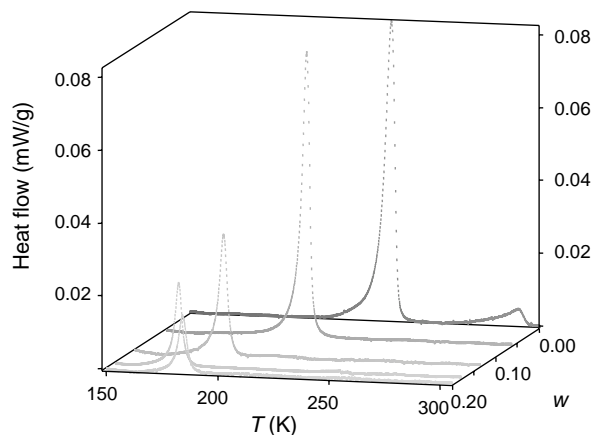

FIG. 1. SmBaFe$_2$O$_{5+w}$: thermal effects (endothermic upon heating) versus temperature and oxygen nonstoichiometry $w = -0.001, 0.064, 0.137, 0.181$ and 0.202.
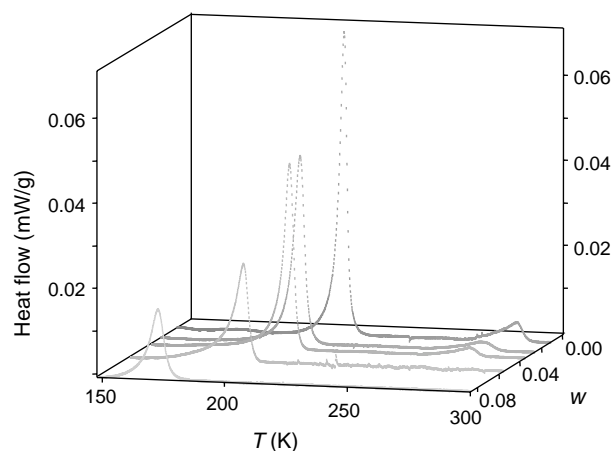
FIG. 3. NdBaFe$_2$O$_{5+w}$: thermal effect (endothermic upon heating) versus temperature and oxygen nonstoichiometry $w = 0.012, 0.027, 0.036, 0.056$ and 0.087.
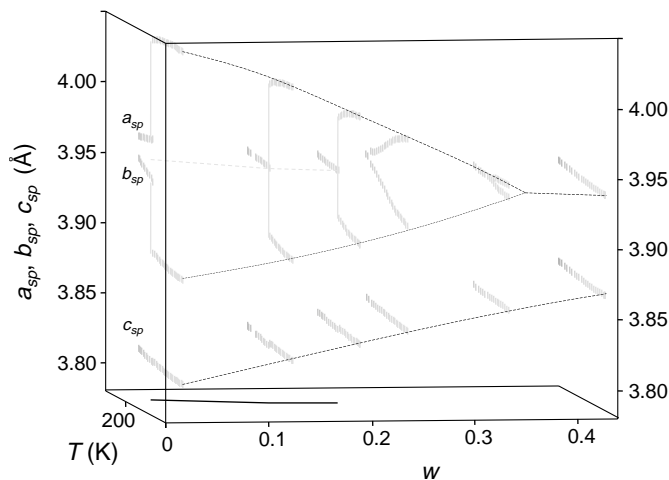
FIG. 2. SmBaFe$_2$O$_{5+w}$: overall variations in single-perovskite-type cell parameters with oxygen nonstoichiometry $w = 0.030, 0.137, 0.202, 0.249, 0.346, 0.439$ and temperature in the range 70–300 K. Plots are situated behind the vertical coordinate planes. T_V is projected on the bottom coordinate plane. Curves are drawn as guides for eye.
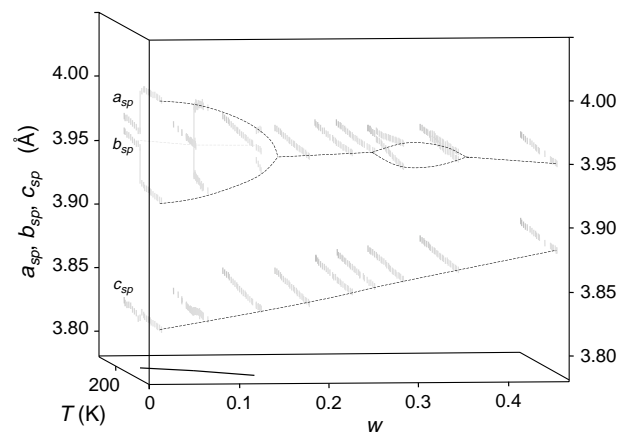
FIG. 4. NdBaFe$_2$O$_{5+w}$: Overall variations in single-perovskite-type cell parameters with oxygen nonstoichiometry $w = 0.027, 0.079, 0.138, 0.192, 0.239, 0.264, 0.296, 0.357, 0.467$ and temperature in the range 70–300 K. Plots are situated behind the vertical coordinate planes. T_V is projected on the bottom coordinate plane. Curves are drawn as guides for eye.

tions, the common charge-ordering character of both transitions steps suggests calling the weaker transition a premonitory one. Figure 2 shows that the charge ordering is accompanied by a profound orthorhombic distortion of the unit cell. This distortion occurs suddenly, but becomes continuous as a function of the nonstoichiometry parameter w. A similar behavior has been observed for Fe_3O_{4+w} (6). In the end, the increased oxygen loading extinguishes the transition altogether at around $w = 0.35$. The latter value is in agreement with the limit when Mössbauer spectra (17) do not reveal any traces of the mixed-valence state above the transition temperature T_V, or of its charge-separated products below T_V. When w approaches zero, a minor orthorhombic distortion appears also for the mixed-valence phase. According to the variable-temperature powder neutron diffraction study (19), this distortion is associated with the onset of the AFM order. As further argued in Ref. (19), Mössbauer data suggest that the premonitory transition is an incomplete charge ordering that happens in the fixed lattice frame of this minor pre-existing structural distortion.

Replacement of Sm^{3+} by the larger Nd^{3+} ion leads to a weaker caloric effect at the main transition (Fig. 3) whereas a stronger one is observed at the premonitory transition. The main transition is now considerably less resistant to oxygen doping (Fig. 4). This suggests that the stability of the charge-ordered state decreases with increasing size of

R^{3+}. In addition, the T_V being lower for $NdBaFe_2O_{5+w}$ indicates a decrease in the stability of the charge-ordered state as compared with the mixed-valence arrangement. Remarkably, around the $w = 0.33$ level for $R = Nd$, another region is observed where the low-temperature phase becomes orthorhombic under a continuous transition. It is quite possible that also this distortion is indicative of charge ordering. In this case we may speculate about five trivalent and one divalent iron atoms (in three unit cells).

The change in the unit-cell metrics under the Verwey transition is illustrated in Figs. 5 and 6 on the respective Nd- and Sm-based samples having oxygen content closest to the pure mixed-valence state. Rietveld refinements of the SXPD cryofurnace data collected at the X7A beamline have been used to extract these temperature dependences. Since the position-sensitive detector was the only alternative for these time-consuming data collections, the precise definition of the diffraction geometry changing with time and temperature has become a major problem considering the delicate changes in the unit-cell dimensions. Diffractometer constants were therefore refined at first and then regressed as a suitable function of temperature to be used in the subsequent unit-cell data refinements. Nevertheless, even this did not prevent occurrences of small sample-independent discontinuities in the unit cell volume curves.
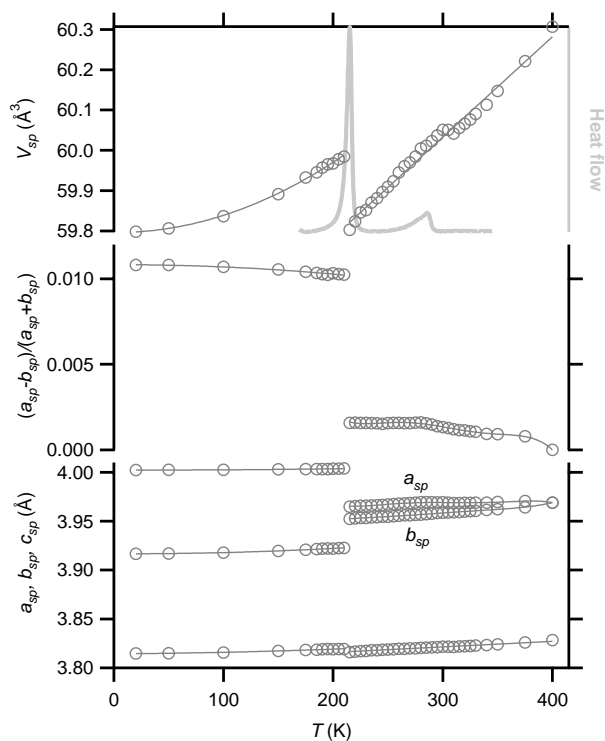

FIG. 5. $NdBaFe_2O_{5.004}$: temperature dependence of the volume, orthorhombic distortion and parameters for a single-perovskite-type cell.
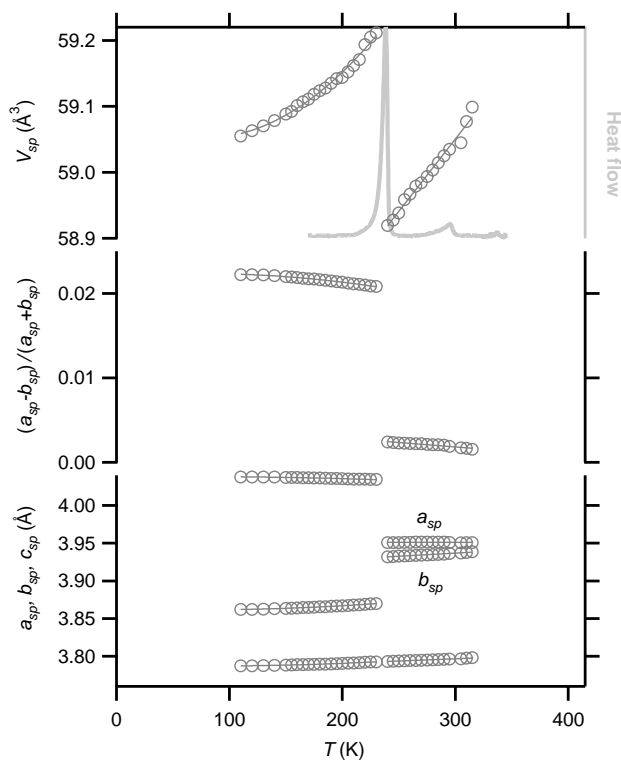

FIG. 6. $SmBaFe_2O_{4.999}$: temperature dependence of the volume, orthorhombic distortion and parameters for a single-perovskite-type cell.

Figures 5 and 6 show that the sudden change in the orthorhombic distortion at T_V (see Figs. 2 and 4) is accompanied by a large, discontinuous change in the unit-cell volume, thereby defining the main transition as a first-order transition. The volume increase occurs upon charge ordering, via an elongation of a which exceeds the contraction of b. This corresponds to the predominant role of one oxygen atom shifting along a in the charge-ordering mechanism (19). A minor difference is seen between the $R =$ Sm and Nd variants in that the latter experiences a distinguishable increase in the unit-cell parameter c upon the charge ordering. This is apparently associated with the more complex structural change occurring for the Nd version, discussed later in Section 3.2. After a careful evaluation of several sets of experimental data, we were not able to determine definitively the volume change which accompanies the premonitory transition. In the case of $R =$ Sm, none of the several minor discontinuities of the volume curves correspond to the premonitory transition, and we conclude no volume change can be detected which exceeds the standard deviations of the experiment. This is in contrast to the minor volume increase reported earlier for $R =$ Tb (19), which appeared slightly larger than standard deviations and coincided (perhaps by chance) with the premonitory transition. However, for $R =$ Nd where the premonitory transition is strongest, Fig. 5 seems to indicate a coincident kink in the temperature dependence of the orthorhombic distortion at the premonitory transition. Even in this case the change is so small that it is unlikely to be definitive.

Two properties typical of first-order transitions are illustrated in Fig. 7: hysteresis and a range of coexistence between the two phases. Considering that T_V decreases with increasing w (see Fig. 1), the tailed shape of the hysteresis curve suggests that a biased distribution of the
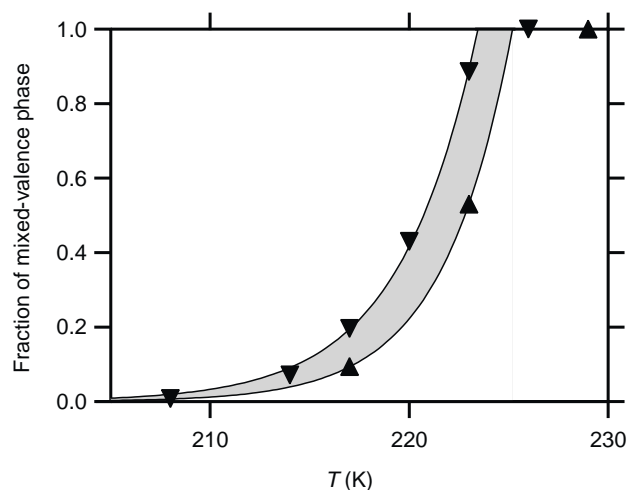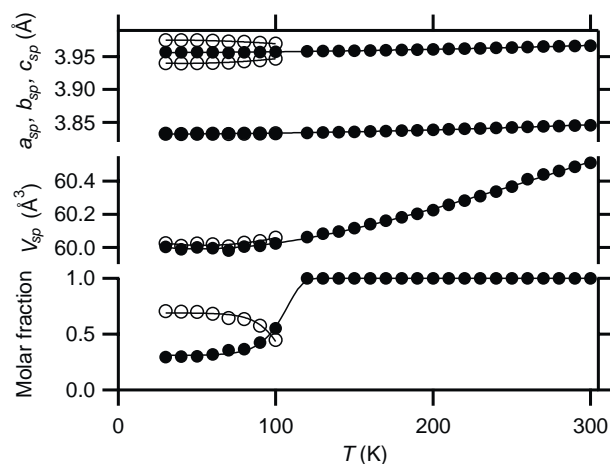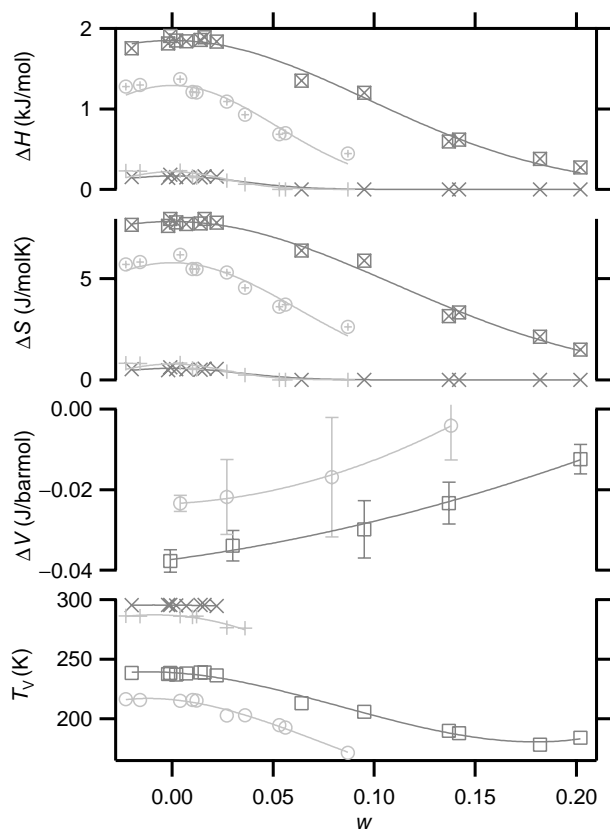

FIG. 8. Transition on the borderline between continuous and discontinuous; molar fraction and single-perovskite-type cell parameters for mixed-valence (full symbols) and charge-ordered (open symbols) $NdBaFe_2O_{5.138}$ from Rietveld refinements.

oxygen contents across the bulk of the sample (a surface oxidation as an example) contributes to this coexistence. Among other factors, distribution of particle sizes springs to mind, the effect of which on T_V has recently been illustrated on magnetite films (24). However, the fairly sharp and reasonably symmetric Bragg peaks suggest that the oxygen-content inhomogeneities are not large. Around the crossover from the transition being discontinuous to continuous as a function of w, the hysteresis widens so that the transition is not fully accomplished in the entire sample even at the lowest tested temperatures (Fig. 8). Also this is likely to be a manifestation of the minor inhomogeneities in w across the samples, say, ± 0.01 in terms of w.

3.1.1. Thermodynamics. The calorimetric and volume data for the Verwey transition in $NdBaFe_2O_{5+w}$ and $SmBaFe_2O_{5+w}$ are plotted in Fig. 9 as a function of the nonstoichiometry parameter w. For sake of consistency, both enthalpy and entropy of the transition were evaluated by integration of the heat-flow-based curves, in case of entropy divided by T, against time. Hence entropy is calculated for each DSC point, as though the DSC peak widths (Figs. 1 and 3) were solely owing to variations in T_V as a function of the distribution in w within the sample. As argued in the previous section, such a distribution is likely. The composition dependences in Fig. 9 were fitted with zero-centered Gaussian-type curves that approximate the probability function of the mixed-valence state formation under the presence of the added oxygen w, as introduced in Ref. (17). Only the volume data have been fitted with three-term polynomials. Data referring to the ideal composition $w = 0.000$ are evaluated from these fits and are listed in Table 3. The total transition entropy for $NdBaFe_2O_{5.000}$ is $\Delta S = 5.79(11)$ J mol^{-1} K^{-1} and for

FIG. 7. Hysteresis of the valence mixing/separation in $SmBaFe_2O_{5.030}$. Orientation of triangles indicates cooling (down) and heating (up).

FIG. 9. $R\text{BaFe}_2\text{O}_{5+w}$ (R = Nd gray lines, $\bigcirc$ and $+$, R = Sm black lines, $\square$ and $\times$): thermodynamic parameters of the charge-ordering transition: premonitory (crosses), main (open symbols) alternatively total (combined symbols). Standard deviations that exceed the size of the symbols are marked.
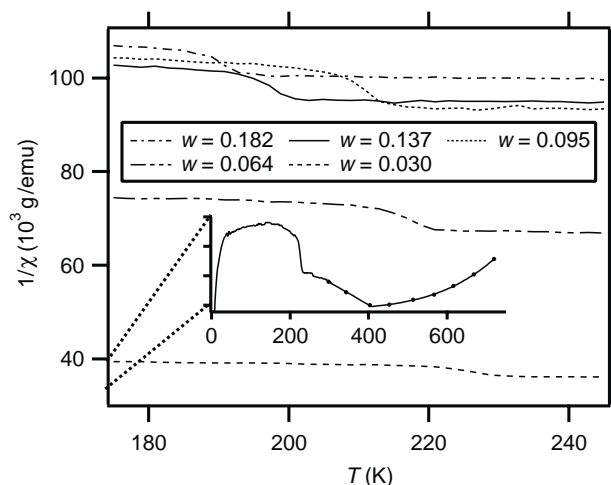
TABLE 3

Thermodynamics of the Premonitory and Main Charge-Ordering Transition for $R\text{BaFe}_2\text{O}_{5.000}$ as Fitted in Fig. 9. Standard Deviations in Parentheses Refer to the Fits.

R	Premonitory	Main
Nd		
T_V (K) (peak value)	286.3(3)	216(1)
ΔV (J bar^{-1} mol^{-1})	practically 0	$-0.0235(6)$
ΔH (kJ mol^{-1})	0.22(3)	1.07(4)
ΔS (J mol^{-1} K^{-1})	0.79(10)	5.00(1)
T_V (K) (peak center value[a])	281(67)	214(14)
dP/dT_V (bar K^{-1})[b]		$-211(4)$
Sm		
T_V (K) (peak value)	295.3(2)	239(1)
ΔV (J bar^{-1} mol^{-1})	practically 0	$-0.0373(10)$
ΔH (kJ mol^{-1})	0.168(7)	1.68(2)
ΔS (J mol^{-1} K^{-1})	0.57(2)	7.26(8)
T_V (K) (peak center value[a])	294(24)	232(6)
dP/dT_V (bar K^{-1})[b]		$-189(2)$

[a] As given by $\Delta H/T = \Delta S$.
[b] By Clapeyron equation as $\Delta H/(T_V \Delta V)$.

3.1.2. Magnetic Susceptibility. A typical magnetic susceptibility curve is illustrated in the inset of Fig. 10. The combined magnetometer SQUID and Faraday balance data for $\text{SmBaFe}_2\text{O}_{5.030}$ show a somewhat peculiar shape that can be understood as an overlap of the AFM susceptibility due to the iron atoms with the paramagnetic susceptibility of Sm^{3+}, one of the weakest magnets among trivalent lanthanoid ions ($gJ = \frac{5}{7}$). The Sm^{3+} ion accounts for the high susceptibility at the lowest temperatures, but its magnetic moment is weak enough for the susceptibility change at the Verwey-type transition to prevail. This change is due to the iron atoms and becomes very difficult to observe when the stronger paramagnetic Nd^{3+} ion

$\text{SmBaFe}_2\text{O}_{5.000}$ $\Delta S = 7.83(10)\,\text{J mol}^{-1}\text{K}^{-1}$. Their difference far exceeds the standard deviations estimated from plots in Fig. 9. When compared with the transition entropy for the $R =$ Tb variant in Ref. (19), $\Delta S = 9.27(11)\,\text{J mol}^{-1}\,\text{K}^{-1}$, a clear dependence of a decreasing transition entropy with increasing ionic size of R^{3+} emerges. This variation excludes application of a simple statistical entropy formula. Nevertheless, the transition entropies are in the same range as the Verwey entropy of magnetite, Fe_3O_4, which also refers to one mixed-valence Fe^{2+}, Fe^{3+} pair. However, the magnetite data in literature suffer with a considerable spread, and we did not attempt to evaluate their reliability. Solely for illustration of the magnitude we have chosen $\Delta S = 7.67\,\text{J mol}^{-1}\,\text{K}^{-1}$ from Ref. (25). Since the tetrahedral spinel sites in magnetite do not participate in the charge ordering/mixing, the volume contraction upon warming through the Verwey transition is much smaller than for $R\text{BaFe}_2\text{O}_5$. As an example, single-crystal data (26) give $\Delta V = -0.0026\,\text{J bar}^{-1}\,\text{mol}^{-1}$, whereas a neutron powder diffraction study (27) gives an even smaller value, $\Delta V = -0.0007\,\text{J bar}^{-1}\,\text{mol}^{-1}$ of Fe_3O_4.
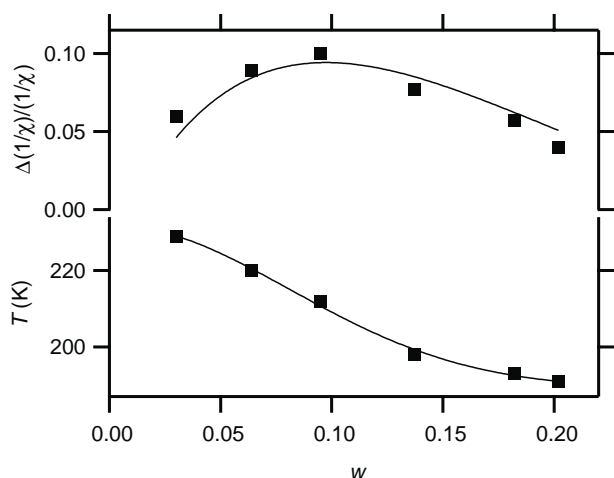

FIG. 10. Magnetic susceptibility change at T_V for selected $\text{SmBaFe}_2\text{O}_{5+w}$ samples. Inset illustrates the full temperature range for the $w = 0.030$ sample ($T_N = 405$ K).

$(gJ = \frac{36}{11})$ is present. Neither could it be discerned (19) for TbBaFe$_2$O$_{5+w}$ ($gJ = 9$ for Tb^{3+}).

A small increase in magnetic susceptibility is observed at the transition into the mixed-valence state for many of the nonstoichiometric SmBaFe$_2$O$_{5+w}$ samples. This is shown in more detail in Fig. 11 (top) where the relative change in the reciprocal susceptibility is plotted versus the nonstoichiometry parameter w, showing a maximum around $w = 0.10$. An explanation for this maximum is offered in Ref. (17) by assuming that the disruption of the magnetic order refers to that portion of the mixed-valence state which is involved in the fluctuating competition of the surrounding square-pyramidally coordinated Fe^{3+} to mix with the minority Fe^{2+}. Finally, we note that the presence of a magnetic susceptibility change at the transition suggests a magnetoresistance effect, which has indeed been observed (28) for SmBaFe$_2$O$_{5+w}$.

3.1.3. Electrical Transport Properties.

Figure 12 shows resistivity versus temperature data for several RBaFe$_2$O$_{5+w}$ compositions with $R =$ Nd and Sm. A sharp upturn in the resistivity is observed where the discontinuous transition is identified by other methods, indicative of the charge-ordering transition. The magnitude of the change for the $R =$ Sm samples is comparable to that of pure Fe$_3$O$_4$ (29,24), for $R =$ Nd it is accordingly smaller, hence possibly correlating with the magnitudes of the transition entropies for these phases. In addition, the resistivity of the SmBaFe$_2$O$_{5.030}$ sample exhibits a proportionally smaller change over the interval 250–295 K where the premonitory transition occurs. This is not seen for the other $R =$ Sm samples in Fig. 12, which do not show the premonitory transition.
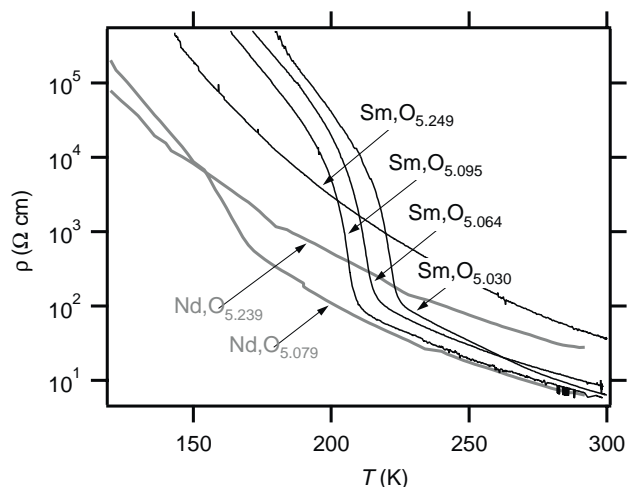
FIG. 12. Electrical resistivity of RBaFe$_2$O$_{5+w}$ as a function of temperature.

Absence of any abrupt conductivity change for samples with high values of w correlates with the structural transition being either continuous (as for $R =$ Sm, $w = 0.249$) or absent (as for $R =$ Nd, $w = 0.239$). Additional data obtained for $R =$ Nd ($w = 0.357$ and 0.402) but not shown in Fig. 12 suggest that the resistivity increases toward the intrinsic Fe^{III} situation with $w = 0.500$. It is also rather high when w approaches zero in the charge-ordered state at low temperatures where localized electronic states are dominant. The conductivity of the mixed-valence phase has maximum for a composition somewhere in the interval $0.00 < w < 0.10$, possibly for the same reason as the maximum in the magnetic susceptibility change, viz., maximum fluctuations in competition to form the mixed-valence state. However, the nonstoichiometry dependences of the conductivity may be rather complex due to contributions from both the mixed valence state and the oxygen doping. An extended study of the defect structure of the oxide would be needed to reveal the defect sources and concentrations. Considering the relatively low temperatures, it is safe to assume that electronic and not ionic carriers participate, and that their concentration is not dependent on temperature. The latter assumption is based on the fact that the samples are heavily doped with respect to the intrinsic situation, and that no oxidation occurred upon cooling below room temperature under the conductivity measurements. This means that the temperature variations can be considered as being due to mobility only. The evaluated Arrhenius activation energy values vary only modestly, from $E_A = 0.0733(3)$ eV for mixed-valence states of the $R =$ Sm samples with $w = 0.064$ and 0.095 to $E_A = 0.0990(6)$ eV for the charge-ordered states. Activation energies for other compositions vary between these values, as an example, $E_A = 0.0839(6)$ eV for $R =$ Nd, $w = 0.402$. These values are consistent with the hopping

FIG. 11. End temperature (bottom) and relative magnitude (top) of the change in reciprocal magnetic susceptibility upon heating for selected SmBaFe$_2$O$_{5+w}$ samples.

regime typical of a doped oxide above T_V as contrasted with the somewhat more strongly localized nature in the charge-ordered state. Accordingly, all samples behaved as semiconductors at the temperatures in question.

3.2. Crystal Structure of Charge-Ordered NdBaFe₂O₅

The sharp upturn in the electrical resistivity and the strong lattice response at the Verwey transition proper are characteristic of a charge-ordering transition. Mössbauer studies (17) also indicate the emergence of distinct di- and trivalent iron states in equal concentrations. For samples with least deviation from the ideal stoichiometry ($w = 0$), the charge order is long range and three dimensional. In the SmBaFe₂O₄.₉₉₉ sample we identified such a 3D order by observing the same weak superstructure Bragg reflections as those observed for TbBaFe₂O₅ in Ref. (19). In this case the charge ordering of the *Pmmm* mixed-valence structure is achieved through a shift of two oxygen sites upon lowering the symmetry to the space group *Pmma*: the apical oxygen and the oxygen atom connecting the square-pyramidal iron coordinations along *a*. However, the observed SXPD reflections are too weak to provide a reliable refinement of the charge-ordered structure, and hence high-resolution powder neutron data were used in Ref. (19) for the structural determination. Unfortunately, this option is not viable for SmBaFe₂O₄.₉₉₉ due to the high absorption cross section of Sm to neutrons.

Rather unexpectedly, relatively strong superstructure Bragg reflections emerged in the low-temperature SXPD pattern of NdBaFe₂O₅.₀₀₄. Compared to the Sm variant, the superstructure Bragg reflections were approximately ten times stronger, and not of the same reflection-condition pattern although indexable on the same unit cell. An

example of the difference is illustrated in Fig. 13. Owing to the favorable intensities, solution of this new super-structure was attempted on the basis of the SXPD data. With the underlying charge-ordering physical process in mind, atomic coordinates of the atoms were released on a trial basis for symmetries of several subgroups of the parent space group *Pmma*. During this investigation we obtained the best fit to the superstructure reflections using a structural model with the *P2₁ma* symmetry (this nonstandard setting of the *Pmc2₁* space group, number 26, is preferred owing to the direct relation to the *Pmma* standard orientation). With the *P2₁ma* model it was possible to refine the atomic coordinates with reasonable accuracy. Due to the loss of symmetry elements, including a mirror plane and the inversion centers, the two special positions do not constrain the atom coordinates in more than just one direction, viz., along the short orthorhombic axis. This means that all atoms are free to shift along the orthorhombic axis *a* that was doubled under the charge ordering, whereas this was possible only for the O(3) atoms under the *Pmma* symmetry. Another consequence of the reduced symmetry is that the Ba and Nd coordinates are no longer completely rigid. However, the Ba *x* coordinate showed no tendency to shift from zero and was subsequently fixed to prevent correlations with other coordinates. A comparison of Figs. 14 and 15 highlights the differences between the charge-ordered structure of the $R = $ Tb, Sm type and the charge ordering in NdBaFe₂O₅.₀₀₄.

The comparison of the observed and fitted SXPD pattern is shown in Fig. 16. The refinement results for the NdBaFe₂O₅.₀₀₄ are given in Table 5, interatomic distances and bond-valence estimates are in Table 4. When the Rietveld refinement is attempted in the frame of the more
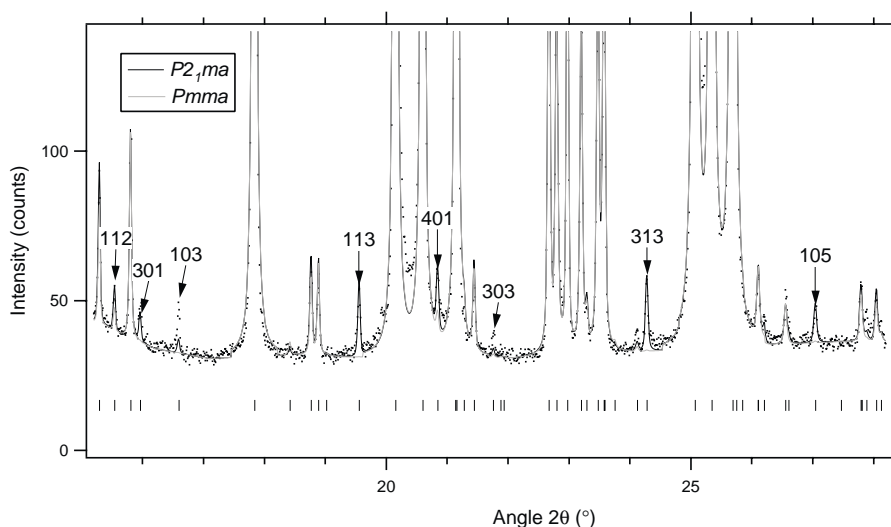

FIG. 13. Examples of reflections whose intensities significantly differ between the NdBaFe₂O₅-type (*P2₁ma*) and the TbBaFe₂O₅-type (*Pmma*) charge-ordered structure.

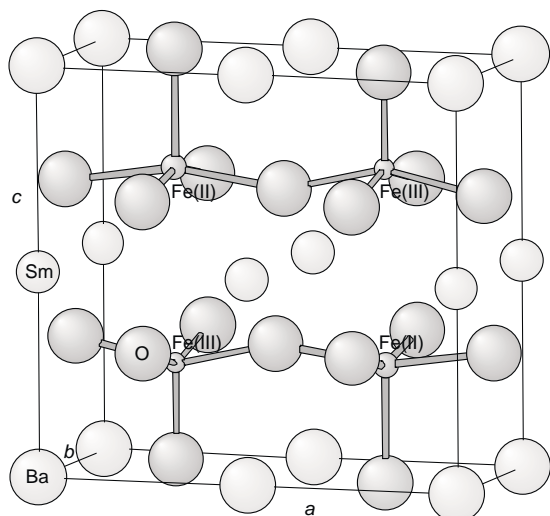**FIG. 14.** The $TbBaFe_2O_5$-type charge ordering (space group *Pmma*), applicable for $SmBaFe_2O_5$.

restrictive *Pmma* space group, figures of merit decay by approximately 0.01, reflecting the poor fit to the superstructure peaks. This exercise not only shows the inadequacy of the *Pmma* model, it also provides insight into the underlying cause for the more profound deformation of the coordination polyhedra in the Nd variant. The z-parameters of the O(1) and Fe(1) atoms experience the most significant change upon going from the symmetry-constrained *Pmma* model ($z = \frac{1}{4}$) to the $P2_1ma$ model. Bond-valence calculations on the refined *Pmma* structure reveal that both O(1) and Fe(1) are overbonded, with bond-valence sums of 2.3 and 3.2, respectively. The origin of this must be in the Nd^{3+} ion, and a comparison of Figs. 2 and 4
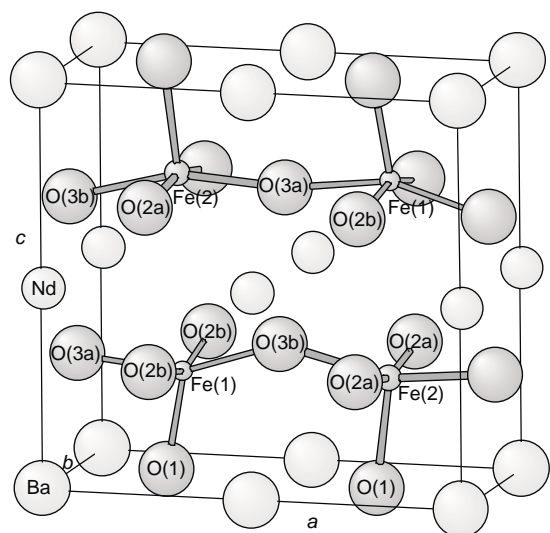

FIG. 15. The structure of charge-ordered $NdBaFe_2O_5$ (space group $P2_1ma$).

shows why. The large size of Nd^{3+} in the a, b mesh does not allow the latter to deform orthorhombically in such a profound manner as seen for $R = $ Sm. This means that the O(3) shift along the longer orthorhombic axis carries less of the bond-valence change, leaving more of the task to the Fe–O(1) bond. Allowing cation displacements from symmetry-fixed positions, the $P2_1ma$ symmetry relaxes the Fe(1)–O(1) distance in exchange for a slight overbonding of the Ba atom (2.12 versus 2.03, Table 4). It is quite intuitive that the structure chooses to overbond the large, soft and polarizable Ba^{2+} ion in order to obtain a more favorable Fe–O bonding interaction.

3.3. Oxygen Loading versus Charge Ordering

The charge-ordered structure represents a 3D cooperative distortion emanating from local distortions of the iron-centered square pyramids. Both oxygen loading (increased w) and valence mixing (increased T) degrade the long-range cooperative nature of these distortions. The former effect must be attributed to local perturbations from the added oxygens w and is reflected in the quick extinction of superstructure reflections in the low-temperature diffraction patterns as w increases. However, the first-order character of the transition, illustrated in Figs. 2 and 4 by a sudden change in both the volume and the orthorhombic distortion, persists up to much higher levels of oxygen loading. Therefore, one must assume that (a) the local distortions of the FeO_5 pyramids that are present when w is approximately zero are also present for higher values of w, and (b) these distortions must remain ordered in one dimension in order to retain the dramatic increase in the orthorhombic distortion. In an attempt to better understand the structural implications of oxygen nonstoichiometry, SXPD patterns were collected at 70 K for several compositions between $0 < w < 0.5$.

No superstructure reflections were detected for $w \geq 0.027$, hence all information must be extracted from refinements of the average structure. In the absence of 3D charge order in the oxygen-loaded samples, the same double-volume perovskite unit cell (space group *Pmmm*; in a limiting case $P4/mmm$) can be adopted for all temperatures and oxygen contents. Such a cell with the appropriate atom labeling is shown in Fig. 17. In order to accommodate for the disorder that accompanies the insertion of the added-oxygen fraction w at the O(4) site, a split-site model was adopted by introducing a Fe' site $\frac{1}{2}, \frac{1}{2}, 0.2500$ with occupancy corresponding to w. An analogous splitting of the O(2) and O(3) sites was omitted in the Rietveld refinements owing to the low scattering contribution from oxygen in general. Under the refinements, the z coordinates of the two O(2) and O(3) orthorhombic sites typically refined to very similar values and were therefore constrained to be equal. The essential structural parameters obtained in the
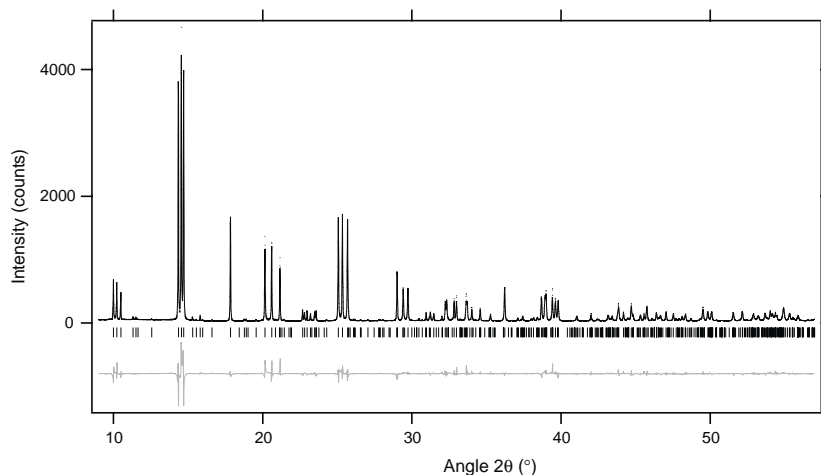
FIG. 16. Rietveld-refinement profile of SXPD data for $NdBaFe_2O_5$ at 15 K.

Rietveld refinements are listed in Tables 6 and 7 for $R = Nd$ and Sm, respectively. Since only the Fe–O(3) distances (and to a lesser extent the Fe–O(1) distances) deviate strongly from their values in the full 3D charge-ordered model, important trends can be extracted from the refined data. As the Fe–O(3) distance decreases with increasing w, the Fe–O(1) and Fe–O(2) distances remain nearly constant in the composition region over which the charge-ordering transition is observed (see Figs. 2 and 4). Such behavior is consistent with the charge separation where the Fe–O distances in the b and c directions are very similar for Fe^{2+} and Fe^{3+}, but the Fe–O distances in the a direction are very different for the two locally nonequivalent iron sites. Since the incorporation of the excess oxygen will convert some of the divalent iron to trivalent iron, the primary effect should be an increase in the number of the Fe^{3+}–O(3) bonds at the expense of the Fe^{2+}–O(3) bonds. Since the former are expected to be shorter than the latter, this should lead to a decrease in the average Fe–O(3) distance, viz., along x. By comparison the average Fe–O(2) and Fe–O(1) distances

along the other two directions should be relatively insensitive to the excess oxygen.

The existence of a first-order transition in a sample such as $SmBaFe_2O_{5.202}$, where 40% of Fe^{2+} in the charge ordered state has been replaced by Fe^{3+}, is quite remarkable. In $(Nd_{0.5+x}Sr_{0.5-x})MnO_3$ no charge ordering is observed when $x > 0.03$ (30,31). In $(R_{0.5-x}Ca_{0.5+x})MnO_3$ charge ordering is observed over a relatively wide range of x, but the transition is of a second (or higher) order and is accompanied by a considerable peak broadening, characteristic of small ordered domains (32). Considering the significant changes in iron–oxygen bond distances that accompany the transition, one would expect that increasing the oxygen nonstoichiometry will introduce significant lattice strain (at least in the x direction). In order to look

TABLE 4
Bond Distances (Å) and Bond Valences for Charge-Ordered $NdBaFe_2O_5$ at 15 K

Atom	Ba	Nd	Fe(1)	Fe(2)	Oxygen BV
O(1)	$2 \times 2.67(1)$		1.87(4)	2.10(4)	2.17
	$2 \times 2.93(1)$				
O(2a)	3.02(7)	2.54(6)		$2 \times 1.98(1)$	1.95
	3.04(7)	2.50(6)			
O(2b)	3.07(6)	2.48(6)	$2 \times 1.99(1)$		2.00
	3.02(6)	2.54(6)			
O(3a)	$2 \times 2.90(2)$	$2 \times 2.53(1)$	2.03(4)	2.05(4)	1.92
O(3b)	$2 \times 3.21(2)$	$2 \times 2.37(1)$	1.96(4)	2.13(4)	2.07
Metal BV	2.12	2.94	2.87	2.17	

TABLE 5
Refinement Results for Charge-Ordered $NdBaFe_2O_5$ at 15 K

Unit-cell data			Statistics	
Space group	$P2_1ma$	R_{wp}		0.117
a (Å)	7.99181(6)	R_p		0.086
b (Å)	3.90985(3)	R_{F^2}		0.074
c (Å)	7.61789(6)	N_{obs}		398
Volume (Å^3)	238.034(2)	N_{vars}		30

Atom	Site	x	y	z	U_{iso}[a] (Å^2)
Nd	2a	0.0074(6)	0	0.4936(8)	0.0062(7)
Ba	2a	0[b]	0	0.0026(8)	0.0039(7)
Fe(1)	2b	0.2665(10)	$\frac{1}{2}$	0.2536(22)	0.0023(7)
Fe(2)	2b	0.7580(15)	$\frac{1}{2}$	0.2620(19)	0.0023(7)
O(1)	2b	0.2269(25)	$\frac{1}{2}$	0.011(5)	0.002(2)
O(2a)	2a	0.750(7)	0	0.299(9)	0.002(2)
O(2b)	2a	0.258(7)	0	0.301(9)	0.002(2)
O(3a)	2b	0.014(4)	$\frac{1}{2}$	0.2834(24)	0.002(2)
O(3b)	2b	0.500(5)	$\frac{1}{2}$	0.3315(25)	0.002(2)

[a] Constrained equal for Fe(1) and Fe(2) and equal for all oxygens.
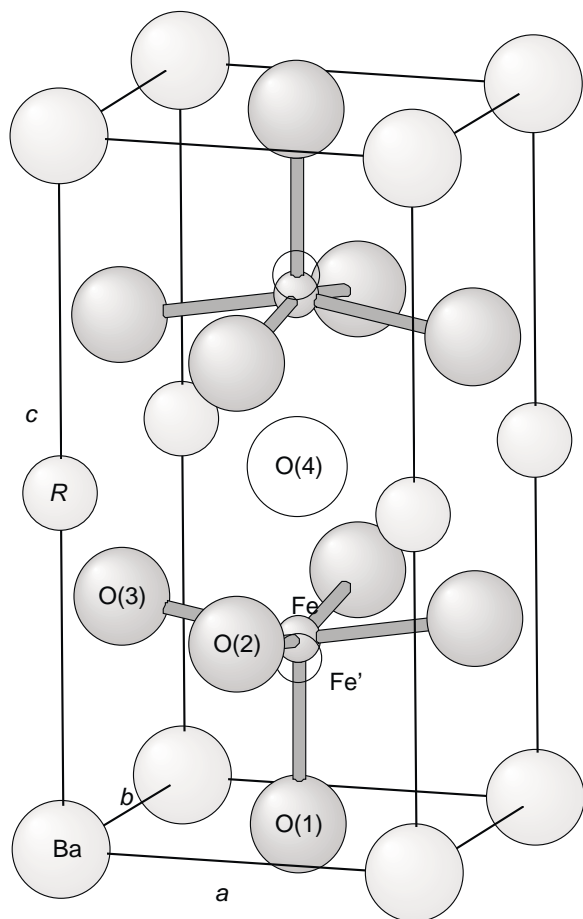[b] Fixed to zero to prevent correlations with other parameters.

FIG. 17. Structural model of oxygen nonstoichiometry in $R\text{BaFe}_2\text{O}_{5+w}$ for refinements from SXPD data.

for the presence of strain and/or small domain size in the 70 K data sets the widths (FWHM) of the 100, 200, 010, 020, 001 and 002 reflections were determined. Surprisingly, the widths were nearly resolution limited (0.01–0.025, in 2θ) and showed almost no compositional dependence, except for a very small, but systematic increase in the strain values for the $h00$ reflections (a maximum of 0.0006), associated apparently with the frustration of the charge ordering. Like the persistence of the first-order phase transition, the general lack of strain in these highly nonstoichiometric samples is quite unexpected.

4. DISCUSSION

In $R\text{BaFe}_2\text{O}_5$, there is an intrinsic conflict between the overall symmetry of the structural framework, where all iron atoms adopt square-pyramidal coordination, and the presence of two integer valence states of iron. The response is charge ordering at low temperatures and valence mixing at high temperatures, linked by the Verwey-type transition. Both states simultaneously decay under increased oxygen loading in $R\text{BaFe}_2\text{O}_{5+w}$. As shown by Mössbauer spectro-

scopy (17), the concentration of $Fe^{2.5+}$ decreases progressively as a function of increasing w. This happens through diminishing both the concentration and the steric availability of the minority Fe^{2+} ions capable of mixing their charge in equal proportion with a neighboring Fe^{3+} ion. The same decrease is observed for the concentrations of the valence- and spin states that constitute the charge-ordered arrangement, hence there is a charge-ordered/ mixed-valence system on one side and a charge-disordered system on the other side evolving as a function of the oxygen nonstoichiometry w. The charge-ordered/mixed-valence transition is controlled by temperature, but depends on w as well. The variation in T_V as a function of w may be taken as a measure of the relative stability of the charge-ordered state versus the mixed-valence state. The decrease in T_V shown in Fig. 9 suggests an initial stability decrease as a function of increasing w. A likely explanation for this behavior is that the excess oxygen converts Fe^{2+} into Fe^{3+}, thereby reducing the Coulombic stabilization of the charge-ordered state.

The mixed-valence/charge-ordered $R\text{BaFe}_2\text{O}_{5+w}$ is remarkably immune to the oxygen loading. Why is this so? For a judgement in this question it is sufficient to consider the stability of the low-temperature charge-ordered state, where the two different iron valences would in particular be expected to create a destabilizing lattice strain. The structural arrangement dictates and Mössbauer data (17) confirm that when the oxygen nonstoichiometry increases from $w = 0$, the five-coordinate Fe^{2+} is being replaced by a six-coordinate Fe^{3+}. The absence of strain in highly nonstoichiometric samples implies that square pyramidal Fe^{2+} can be exchanged with octahedral Fe^{3+} without significantly disturbing the surrounding lattice. A similar argument would be valid for the replacement of five-coordinate $Fe^{2.5+}$ ions in the mixed-valence variant. Since the Fe–O(4) bond that completes this exchange is a short one (toward the added oxygen in the R layer) it carries the majority of the bond-valence increase necessary to form the trivalent iron. The residual imbalance can be dealt with by minor distortions of the polyhedra. Undoubtedly, this structural feature is critical to the unusually large compositional range over which the first-order Verwey-type transition into the charge-separated state is observed in the $R\text{BaFe}_2\text{O}_{5+w}$ phases. It also gives a clue about the effect of the R^{3+} ion size; when Sm is replaced by the larger Nd, the Fe–O(4) bond becomes longer and carries less bond valence. Therefore, the particular octahedron which replaces the square pyramid is forced to become increasingly distorted. This local distortion diminishes the compositional range over which a first-order transition to the charge-ordered state is observed for the large R atoms such as Nd.

The occurrence of the Verwey transition is a rather special phenomenon. Either the mixed-valence or the

TABLE 6
Structure Parameters for NdBaFe$_2$O$_{5+w}$ at 70 K According to Rietveld Refinements

w	0.027	0.079	0.192	0.239	0.264	0.296	0.357
R_{F^2} (%)	5.95	6.20	6.27	6.24	8.26	6.37	5.60
Unit-cell parameters							
a (Å)	4.00064(5)	3.99137(5)	3.95107(2)	3.94980(5)	3.95123(2)	3.96077(3)	3.95370(1)
b (Å)	3.91976(4)	3.92309(4)	—	—	a	3.94182(3)	3.94810(1)
c (Å)	7.63805(9)	7.64604(9)	7.67112(4)	7.6821(1)	7.6914(1)	7.70688(4)	7.72428(3)
Volume (Å^3)	119.776(3)	119.726(3)	119.754(2)	119.847(5)	120.080(5)	120.325(2)	120.573(1)
Atom positions	*Pmmm*	*Pmmm*	*P4/mmm*	*P4/mmm*	*P4/mmm*	*Pmmm*	*Pmmm*
z(Fe)	0.2570(6)	0.2575(7)	0.2570(4)	0.255(1)	0.254(1)	0.2535(7)	0.2531(6)
z[O(2)/O(3)]	0.3038(7)	0.3017(9)	0.2992(5)	0.297(2)	0.254(1)	0.2973(7)	0.294(1)
Displacement parameters B_{iso} (Å^2)							
Ba	0.49(7)	0.45(7)	0.28(4)	0.6(2)	1.2(1)	0.43(6)	0.28(4)
Nd	0.36(6)	0.48(6)	0.73(4)	1.2(2)	1.2(1)	0.98(6)	0.65(4)
Fe	0.64(5)	0.48(4)	0.47(2)	0.6(2)	1.2(1)	0.53(3)	0.23(2)
O	0.24(16)	0.79(16)	0.95(8)	1.2(4)	1.2(3)	1.42(8)	0.6(1)
Bond distances (Å)							
Fe–O(1)	1.963(5)	1.969(5)	1.972(3)	1.963(9)	1.957(7)	1.954(5)	1.955(5)
Fe–O(2)(2×)	1.992(1)	1.991(2)	2.002(3)	2.000(3)	2.003(2)	2.000(1)	1.999(2)
Fe–O(3)(2×)	2.031(1)	2.024(2)	2.002(3)	2.000(3)	2.003(2)	2.009(1)	2.010(2)

Pmmm: Nd $[0, 0, \frac{1}{2}]$, Ba $[0, 0, 0]$, Fe $[\frac{1}{2}, \frac{1}{2}, z]$, Fe' $[\frac{1}{2}, \frac{1}{2}, 0.25]$, O(1) $[\frac{1}{2}, \frac{1}{2}, 0]$, O(2) $[\frac{1}{2}, 0, z]$, O(3) $[0, \frac{1}{2}, z]$, O(4) $[\frac{1}{2}, \frac{1}{2}, \frac{1}{2}]$.
P4/mmm: same positions except that O(2)≡O(3).
Constraints: z[O(2)] = z[O(3)], B_{iso} equal for all oxygens.
[a] A two-phase sample: 22% orthorhombic, *Pmmm*, $a = 3.9711(2)$, $b = 3.9311(2)$ and $c = 7.6996(3)$ Å.

charge-ordered arrangements alone would be sufficient to solve the structural dilemma introduced above. The fact that the charge ordering occurs in two stages is even more remarkable. According to Ref. (19), the premonitory transition is related to the existing orthorhombic deformation in RBaFe$_2$O$_{5+w}$ ($w = 0$), introduced by the onset of

TABLE 7
Structure Parameters for SmBaFe$_2$O$_{5+w}$ at 70 K According to Rietveld Refinements

w =	0.030	0.095	0.137	0.202	0.249	0.346	0.439
R_{F^2} (%)	6.17	8.49	9.41	5.58	5.76	7.91	3.72
Unit-cell parameters							
a (Å)	4.03607(2)	4.02380(3)	4.01151(2)	3.99017(3)	3.97077(4)	3.94040(2)	3.93185(1)
b (Å)	3.87382(1)	3.87907(2)	3.88704(2)	3.89853(2)	3.90722(3)	3.93186(2)	
c (Å)	7.59961(3)	7.61661(5)	7.63363(4)	7.65530(5)	7.66597(6)	7.70020(3)	7.72057(3)
Volume (Å^3)	118.820(1)	118.885(2)	119.030(1)	119.084(2)	118.935(2)	119.300(1)	119.356(1)
Atom positions	*Pmmm*	*Pmmm*	*Pmmm*	*Pmmm*	*Pmmm*	*Pmmm*	*P4/mmm*
z(Fe)	0.2588(4)	0.2578(5)	0.2601(6)	0.2572(8)	0.256(1)	0.2553(6)	0.2560(6)
z[O(2)/O(3)]	0.3079(4)	0.3043(6)	0.3029(7)	0.3036(7)	0.3002(9)	0.3035(6)	0.2943(6)
Displacement parameters B_{iso} (Å^2)							
Ba	0.32(4)	0.56(5)	0.69(7)	0.36(7)	0.24(8)	0.32(4)	0.00(4)
Sm	0.43(3)	0.57(4)	0.84(6)	0.49(6)	0.63(8)	0.89(4)	0.53(4)
Fe	0.64(2)	0.54(4)	0.56(4)	0.16(5)	0.28(6)	0.36(2)	−0.02(2)
O	0.06(7)	0.79(16)	0.71(16)	0.16(16)	0.39(16)	1.58(8)	0.71(8)
Bond distances (Å)							
Fe–O(1)	1.967(3)	1.963(4)	1.985(5)	1.969(6)	1.961(6)	1.966(5)	1.977(5)
Fe–O(2)(2×)	1.973(1)	1.972(1)	1.971(1)	1.981(2)	1.983(2)	2.001(1)	1.988(1)
Fe–O(3)(2×)	2.052(1)	2.043(1)	2.032(1)	2.027(2)	2.014(2)	2.005(1)	1.988(1)

Note. Atom coordinates as in Table 6, constraints: z[O(2)] = z[O(3)], B_{iso} equal for all oxygens.

magnetic order at higher temperatures. This deformation is quickly averaged by the added oxygens w in the a, b mesh, and the premonitory transition disappears. In contrast to the main transition, the caloric effect under the premonitory transition is somewhat larger for $R = $ Nd than for Sm. This suggests a larger extent of the premonitory charge ordering for the variant with the larger Nd atom. Since the premonitory transition utilizes the existing small orthorhombic distortion in a fixed lattice frame, the favorable effect of the large Nd atom is that it allows for a more off-centered position of the oxygen atom in the Fe–O–Fe bridges along the longer orthorhombic axis before a minimum Fe–O distance is reached on the shorter side of the bridge. However, the premonitory attempt fails to fully order the charges. This task is accomplished by the main transition occurring at a lower temperature T_V. The electron localization at T_V occurs through inducing a huge orthorhombic distortion, a process where the large size of Nd becomes a disadvantage. Unable to allow as large orthorhombic distortion as the Sm variant, the Nd atom causes a more extensive deformation of the coordination polyhedra and a larger bond-valence imbalance.

The costly fulfillment of the bond-valence conditions for the charge ordered $NdBaFe_2O_{5.00}$ suggests thermodynamic destabilization of the charge-ordered state as compared with the mixed-valence state, and this is in agreement with T_V being lower for $R = $ Nd than $R = $ Sm. Furthermore, the caloric effect is smaller for $R = $ Nd. The lower transition entropy may be a consequence of the less symmetric $P2_1ma$ structure of the charge ordered state. The lower transition enthalpy may suggest that the extent of the charge-ordering is smaller in $NdBaFe_2O_{5.00}$. Evidence for the latter comes from the observation that high values of T_V correlate with high resistivity in the charge-ordered state (Fig. 12). Thus, a stronger electron localization is implied for smaller R ions. A similar situation is observed in molecular crystals where moieties not explicitly coordinated to the mixed-valence iron are observed to exhibit significant influence on the stability of the charge-ordered state (15). Any explanation of the interesting behavior of these compounds must recognize the fact that both the charge-ordered and the mixed-valence states are cooperative phenomena. Therefore, the Verwey transition itself must also be cooperative in nature, something that has already been illustrated on magnetite thin films, where the transition rapidly disappears below a certain thickness of the film (24).

ACKNOWLEDGMENTS

REFERENCES

1. E. J. W. Verwey, *Nature (London)* **144,** 327 (1939).
2. E. J. W. Verwey, P. W. Haayman, and F. C. Romeijan, *J. Chem. Phys.* **15,** 181 (1947).
3. J. P. Wright, J. P. Attfield, and P. G. Radaelli, *Phys. Rev. Letters* **87,** 266 401 (2001).
4. F. J. Berry, S. Skinner, and M. F. Thomas, *J. Phys.: Condens. Matter* **10,** 215 (1998).
5. T. Yoyoda, S. Sasaki, and M. Tanaka, *Am. Mineral.* **84,** 294 (1999).
6. J. P. Shepherd, R. Aragón, J. W. Koenitzer, and J. M. Honig, *Phys. Rev. B* **32,** 1818 (1985).
7. Z. Kąkol, J. Sabol, J. Stickler, and J. M. Honig, *Phys. Rev. B* **46,** 1975 (1992).
8. R. Aragón and J. M. Honig, *Phys. Rev. B* **37,** 209 (1988).
9. J. P. Shepherd, J. W. Koenitzer, R. Aragón, J. Spałek, and J. M. Honig, *Phys. Rev. B* **43,** 8641 (1991).
10. J. M. Honig, *J. Alloys Comp.* **229,** 245 (1995).
11. V. A. M. Brabers, F. Walz, and H. Kronmüller, *Phys. Rev. B* **58,** 14163 (1998).
12. H. Kloor and J. M. Honig, *J. Solid State Chem.* **148,** 135 (1999).
13. J. H. V. J. Brabers, F. Walz, and H. Kronmüller, *J. Phys.: Condens. Matter* **11,** 3679 (1999).
14. J. P. Attfield, A. M. T. Bell, L. M. Rodríguez-Martínez, J. M. Greneche, R. J. Cernik, J. F. Clarke, and D. A. Perkins, *Nature (London)* **396,** 655 (1998).
15. M. Sorai and D. N. Hendrickson, *Pure Appl. Chem.* **63,** 1503 (1991).
16. G. Wu, Y. Zhang, L. Ribaud, P. Coppens, C. Wilson, B. B. Iversen, and F. K. Larsen, *Inorg. Chem.* **37,** 6078 (1998).
17. J. Lindén, P. Karen, A. Kjekshus, J. Miettinen, T. Pietari, and M. Karppinen, *Phys. Rev. B* **60,** 15251 (1999).
18. P. Karen and P. M. Woodward, *J. Mater. Chem.* **9,** 789 (1999).
19. P. Karen, P. M. Woodward, J. Lindén, T. Vogt, A. Studer, and P. Fisher, *Phys. Rev. B* **64,** 214 405 (2001).
20. I. Barin and O. Knacke, "Thermochemical Properties of Inorganic Substances," p. 316 and 584, Springer, Berlin, 1973.
21. I. Barin, O. Knacke, and O. Kubashevski, "Thermochemical Properties of Inorganic Substances, Supplement," p. 295, Springer, Berlin, (1975).
22. P.-E. Werner, "The Computer Programme SCANPI 9." Institute of Inorganic Chemistry, University of Stockholm, Sweden, 1992.
23. A. C. Larson and R. B. Von Dreele, Los Alamos Laboratory Report LA-UR-86-748, 1987.
24. M. Ziese and H. J. Blythe, *J. Phys.: Condens. Matter* **12,** 13 (2000).
25. S. Takai, Y. Akishige, H. Kawaji, T. Atake, and Sawaguchi, *J. Chem. Thermodyn.* **26,** 1259 (1994).
26. J. Yoshida and S. Iida, *J. Phys. Soc. Jpn* **47,** 1627 (1979).
27. J. P. Wright, A. M. T. Bell, and J. P. Attfield, *Solid State Sci.* **2,** 747 (2000).
28. J. Nakamura, J. Lindén, M. Karppinen, and H. Yamauchi, *Appl. Phys. Lett.* **77,** 1683 (2000).
29. M. Matsui, S. Todo, and S. Chikazumi, *J. Phys. Soc. Jpn.* **42,** 1517 (1977).
30. P. M. Woodward, D. E. Cox, T. Vogt, C. N. R. Rao, and A. K. Cheetham, *Chem. Mater.* **11,** 3528 (1999).
31. Y. Moritomo, T. Akimoto, A. Nakamura, K. Ohoyama, and M. Ohashi, *Phys. Rev. B* **58,** 5544 (1998).
32. N. Kumar and C. N. R. Rao, *J. Solid State Chem.* **129,** 363 (1997).